CrossMark

Automated Fiducial Points Detection Using Human Body Segmentation

Fozia Rajbdad[1] · Murtaza Aslam[1] · Shoaib Azmat[1] ·
Tauseef Ali[2] · Shahid Khattak[1]

Abstract Accurately detected human body fiducial points provide an easy and efficient method for human body posture analysis and the extraction of anthropometric parameters. In the proposed work, an efficient algorithm for automated and accurate detection of fiducial points is developed for both the frontal and the lateral images. An algorithm for automatic human body segmentation of the frontal image is also developed using automatically detected set of primary fiducial points. Additional fiducial points are obtained by applying peak and valley algorithm on the silhouettes of each segment. The detection accuracy of the automatically detected fiducial points is calculated by comparing their locations with the manually marked fiducial points. The proposed algorithm is tested on 45 subjects including both male and female genders and variable Body Mass Indexes. In most cases, the algorithm successfully detects seventy fiducial points for each subject in the testing set. A quantitative analysis of the error in the position of the detected fiducial points shows that the algorithm performs better than the state-of-the-art algorithms found in the existing literature. In the evaluation of the algorithm, the percentage accuracy of the detected fiducial points is calculated and it is observed that the proposed algorithm performs better for the majority of the fiducial points.

Keywords Anthropometric parameters · Fiducial points ·
Frontal · Lateral · Posture · Silhouette

✉ Fozia Rajbdad
 foziarajab@ciit.net.pk

1 Electrical Engineering Department, COMSATs Institute of
 Information Technology, Abbottabad, Pakistan

2 Faculty of Electrical Engineering, Mathematics and Computer
 Science, University of Twente, Enschede, The Netherlands

1 Introduction

In the past few years, many ubiquitous healthcare applications have been developed that employ the anthropometric parameters of a human body using body fiducial points (FPs). A fiducial point (FP) is defined as a significant point on the silhouette of a human body that is useful for automatic measurement of human body parameters like anthropometric measurements, postural disorders, etc. These anthropometric parameters play a significant role in the design of applications in the area of security, medicine, sports and clothing industry. The conventional methods employed for collecting anthropometric data involve manual measurements. This, however, relies heavily on the expertise of the operators, the cooperation of the subject, and requires examiner's time and effort [1]. An automatic anthropometry system is, therefore, needed to accelerate and standardize the process. The FPs from a human body can be used to determine the anthropometric parameters which can, in turn, be used in the construction of 3D human models [2,3] and in recognizing human actions [4–6]. Additionally, it can be used for non-contact body size measurements [7] in the apparel industry, where it can, for example, automatically determine the clothing sizes fit for a consumer [8–11].

Due to the complexity of the problem of human anthropometry, some semi-automated approaches are also proposed. For example, manually marked FPs are used by Dunk et al. [12] for measuring three spinal angles cervical, thoracic and lumbar to evaluate posture disorders in the torso and pelvic regions. Such systems can be made efficient by using automatically detected FPs.

Advanced 3D human body scanning has been employed for the automatic detection of FPs and the measurement of anthropometric parameters [10,13–16]. Although these scanners are quite accurate, they require multiple cameras

Springer

and radar sensors and are therefore limited by cost, maintenance, and mobility [2,17]. Additionally, extracting the useful information from the raw 3D scanner data requires extra post-processing and results in an increased processing time [18]. In [19], contour-based and silhouette-based features have been investigated for automatic detection of the FPs. In this method, the detected FPs are marked sequentially on a single segment making it difficult to associate the detected FPs with a particular body part. Moreover, it has a tendency to detect extra FPs which are then difficult to filter. In [20–22], Scale Invariant Feature Transform (SIFT), Harris-Laplacian, and Speeded-Up Robust Features (SURF) have been used to detect significant points within images. These algorithms can also be used for human body FPs detection, but suffer from the similar error propagation and segment association effects as mentioned for [19].

In [12], the FPs are detected from 2D camera images, by physically placing markers on the body. In [23,24], the FPs are marked manually on the image, while in [25] the system is automatic only for the upper body part. In [26], Lin et al. propose a method for the automatic detection of FPs from 2D images using the silhouette of the human body. In their work, Canny edge detector [27] is applied to trace the contour of the human body, and the Freeman eight-directional chain code [28] is used to represent the human body shape. The FPs are finally detected using the difference between the adjacent codes from the shape contour.

In this paper, a novel method for automatic detection of FPs using 2D images through segmentation is proposed. The input frontal view image of a subject is segmented into six simpler regions in order to improve the detection accuracy. The FPs within each segment are detected using the boundary information. The extracted boundary of each segment is then processed as a single dimensional signal and the local minima and the maxima are detected as the FPs. The lateral view image is considered as a single segment, and FPs are detected using the boundary information. The proposed method not only detects a larger number of FPs but also intelligently identifies the position of detected FPs, and associates them with the body parts automatically using segmentation. All the FPs are detected independently, whereas, in the state-of-the-art work of Lin et al. [26], the chance of incorrect detection is high because the detection of every FP depended on the correct detection of the previous one. Furthermore, the segmentation of the human body helps in an easy and accurate extraction of anthropometric parameters. The FPs detection accuracy is evaluated by calculating the Euclidean distance in centimeters between automatically detected FPs and manually marked FPs. It is found that our proposed algorithm reduces the detection error significantly as compared to Lin's work [26]. Additionally, the percentage accuracy of the proposed algorithm is calculated for all the test subjects and it is also found to be better than Lin's method [26].

Our main contributions and findings in this paper are listed as below:

- We propose a novel method for automatic detection of FPs using 2D images of frontal and lateral views of the human body through segmentation.
- The proposed method automatically detects greater number of FPs compare to state-of-the-art algorithms found in the existing literature and also intelligently associates them with the body parts automatically using segmentation
- The detection accuracy of automatically detected FPs is verified by comparing with manually marked FPs for a range of allowable errors. The proposed algorithm reduces the detection error significantly for the majority of FPs as compared to the state-of-the-art method.

Rest of the paper is organized as follows. Section 2 presents the experimental setup. Section 3 describes in detail our proposed algorithm for automatic FPs detection. Section 4 presents results and discussion showing how our proposed technique performs in comparison with the existing techniques in the literature. We conclude the paper in Sect. 5.

2 Experimental Setup for Body Fiducial Points Detection

Figure 1a shows the setup of the data collection for experiments and analysis. It includes a blue background screen, a dedicated processing unit, and two web-cameras. The blue background screen as shown in Fig. 1b is used for efficient identification of a subject from the background. Eight markers on the screen are used for restoring the dimensions of the image and converting image coordinates to real-world measurements. The distance between the screen and the camera is 250 cm and height of the screen base from the floor is 10 cm. Two web-cameras of 4600×3450 resolution are mounted on a single stand at different levels in order to capture the images of the subjects with different heights. Open computer vision (OpenCV) library [29] is used for interfacing web-cameras and the computer.

2.1 Test Protocol and Dataset

Two photographs—one from frontal view and one from lateral view—are taken. For the frontal view, the subjects are required to keep their limbs straight and arms apart from the torso. It is ensured that the armpit and crotch points of each subject are visible, as these points are later used by the body segmentation algorithm. For the lateral view, the body is kept straight with arms pressed along the torso. Spe-
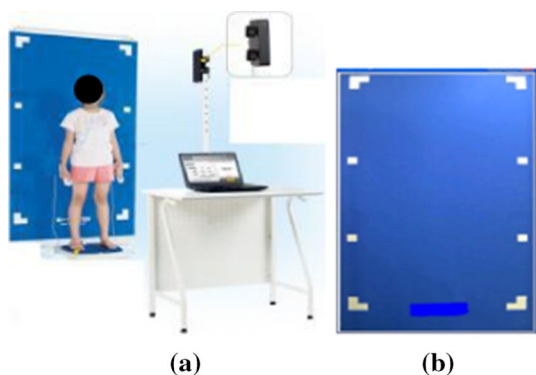
Fig. 1 **a** Overall view of the experimental setup, **b** marker screen

cial measurement attires are used while taking photographs so that most of the curves of the body are clearly visible which are helpful for the detection of body FPs. Similarly, specialized caps are also worn by the subjects in order to reduce the influence of hairs on the test results. The dataset from 45 subjects including 28 females and 17 males aged from 20 to 45 are used for testing the proposed algorithm. Table 1 shows the details of different parameters of the subjects.

2.2 Screen Calibration

The set of eight markers on the screen are used for calibration as shown in Fig. 2. The captured screen image with no subject standing in front of the screen is processed for the detection of screen markers, and the calibrated values of the markers are determined. The screen calibration process is performed only once, and the calibrated values are subsequently used for all the subjects. Figure 2 shows the different steps involved in the screen marker detection process. The RGB image obtained from the camera is converted to YC_bC_r color space where global thresholding is performed on the Chroma (C_b) component in order to identify the screen outline from the complex background. Four corner points of the background screen are detected, and bilinear transformation [30] is applied to the image to remove optical distortions introduced by the position of the camera. The binary image is then divided into eight sub-images of equal sizes, each including one marker and the corner point of each marker is detected. Since the distance between markers is known, these values can be used for transforming image dimensions to the screen's real-world dimensions in centimeters. The ratio of the distance between two corresponding corner points of markers (in pixels) and actual measurement between the same points (in centimeters)

Table 1 Dataset parameters

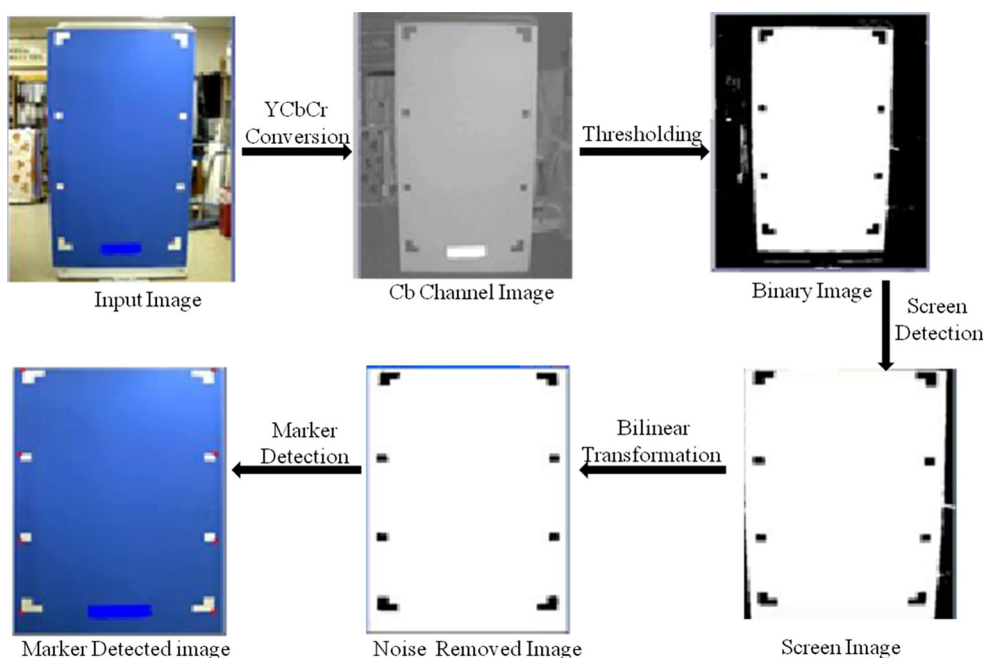| Number of subjects	Sex	Age	Height (cm)	Weight (Kg)	Body Mass Index (BMI)
28	Female	20–45	155–175	55–80	18–35
17	Male	20–45	160–180	60–80	18–35

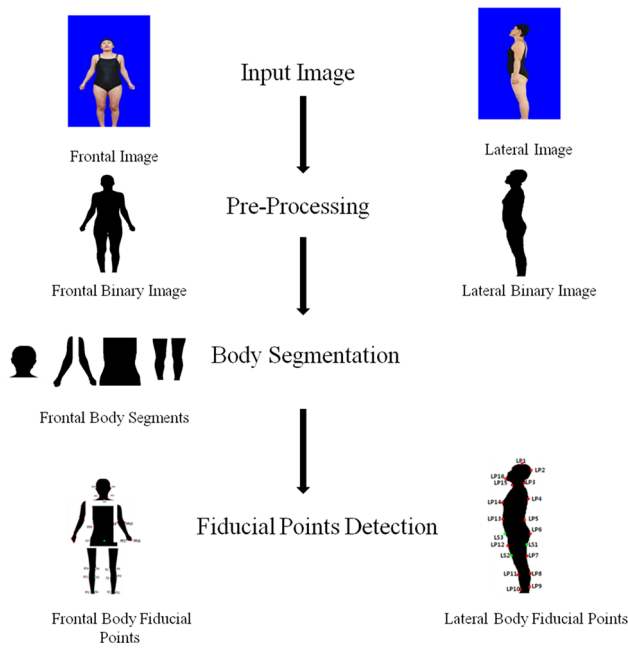**Fig. 2** Overview of the proposed method for calibration

Fig. 3 Overview of the proposed algorithm for body fiducial points detection

is defined as the calibration value. The calibration values for horizontal and vertical dimensions are calculated and saved.

3 Fiducial Points Detection

The proposed algorithm for detection of FPs from frontal and lateral images is summarized in Fig. 3. The acquired image is converted to YC_bC_r color space to separate the subject from the background. The human body segmentation algorithm is applied to divide the body into six segments from the frontal view. Inner and outer boundaries of the segment are extracted. Finally, the FPs of each segment are detected by Peak and Valley algorithm [31]. Note that there is no segmentation

involved in the case of lateral view and it is considered a single segment.
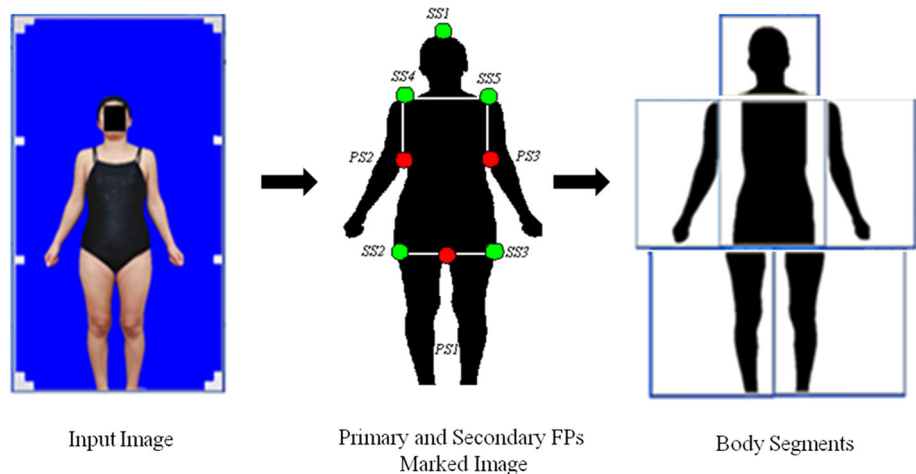
3.1 Pre-processing

The input image of 4600×3450 pixels is resized to a lower resolution of 460×345 pixels in order to speed up the FPs detection process. Bilinear transformation is applied to the subject image using the screen corner points that are detected earlier in the screen calibration process, thereby restoring the dimensions throughout the image. Global thresholding is applied to the restored image in order to find crisp boundaries between the subject and the background screen. The blob detection algorithm described in [32] is finally applied to detect the largest blob, which is the subject.

3.2 Body Segmentation

A human body has a complex structure. The detection of all the FPs at the same time using the entire body frontal image is less accurate due to the sequential nature of the detection algorithms. A body segmentation algorithm is, therefore, proposed which increases the detection accuracy by dividing a human body into smaller segments. Such algorithms can be used for associating the detected FPs with a corresponding body segment and for its localization. Since the search space is restricted to individual segments, the unnecessary detection of FPs in other body parts is avoided and the system becomes more efficient. Also the error propagation effects are restricted to a single segment, as the effect of false detection/omission of FPs does not effect the localization of FPs in the other body segments.

In Fig. 4, the human body segmentation method for the frontal view is illustrated using the red colored primary FPs (PFPs) and green colored secondary FPs (SFPs). The three PFPs are detected using the areas between legs and arms and

Fig. 4 Overview of the proposed method for body segmentation

Input Image

Primary and Secondary FPs Marked Image

Body Segments

(a) Right Arm Inner Boundaries

(c) Primary FP Marked Image

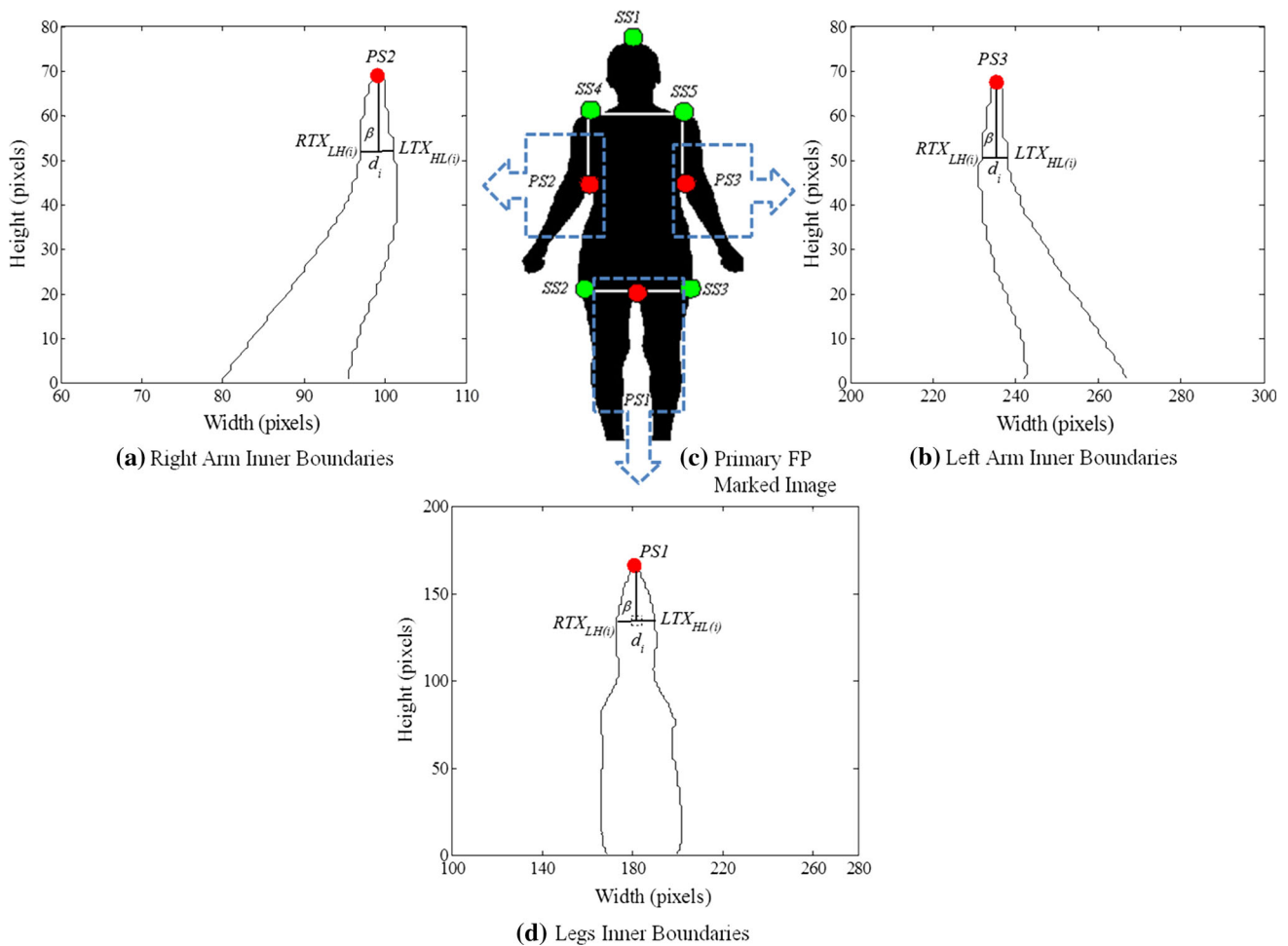**(b)** Left Arm Inner Boundaries

(d) Legs Inner Boundaries

Fig. 5 Primary and secondary fiducial points detection method

are labeled in Fig. 5c as $PS1$, $PS2$, $PS3$. These are then used to detect the SFPs.

To detect the $PS1$, the binary image is scanned from left to right starting from the bottom. RTX_{HL} is the transition of pixel value from high to low (white to black) along the x-axis and indicates the outer boundary of the right leg. The next transition from low to high (black to white) along the x-axis is RTX_{LH}, which indicates the inner boundary of the right leg. Similarly, LTX_{HL} and LTX_{LH} indicate the left leg's inner and outer boundaries, respectively. The image is scanned horizontally one row at a time, starting from the bottom of the image. The scanning stops when the difference between RTX_{LH} and LTX_{HL} becomes less than $\alpha = 5$ pixels, i.e.,

$$d_i = LTX_{HL(i)} - RTX_{LH(i)} < \alpha. \tag{3.1}$$

where $RTX_{LH(i)}$ and $LTX_{HL(i)}$ corresponds to the left and right transitions at ith row of the image.

The crotch point ($PS1$) as shown in Fig. 5d is calculated as,

$$PS1(x, y) = \left(RTX_{LH(i)} + \frac{d_i}{2}, i + \beta \right), \tag{3.2}$$

where β in Eq. (3.2) is the number of pixels in the vertical direction between ith row where Eq. (3.1) is satisfied and the first transition from high to low, as shown in Fig. 5d. Similarly, the right and left armpit points $PS2$ and $PS3$ are detected as shown in Fig. 5a, b. The three PFPs are not sufficient to segment the frontal view of the human body and additional FPs, i.e., SFPs are determined as shown in Fig. 5c. The image is scanned vertically from $PS1$, $PS2$, and $PS3$, the number of pixels $TY_{LH(K)}$ to the first transition from low to high is determined. The kth secondary FP SSK is given as

$$SSK(x, y) = \left(PSK(x), PSK(y) \pm TY_{LH(K)} \right),$$
$$\text{where } K = 1, 4, 5. \tag{3.3}$$

Here, $SS1$ is the head top, $SS4$ is the right clavicle, $SS5$ is the left clavicle, and PSK is the kth PFP. Similarly, two more SFPs, i.e., $SS2$ and $SS3$ are detected by the first transition
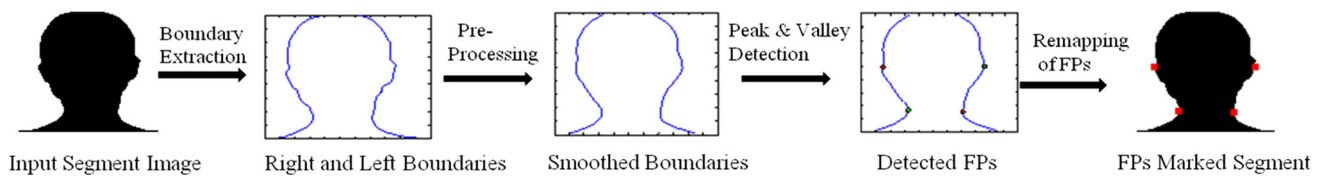
Fig. 6 Overview of the segment's FPs detection

from low to high along x-axis TX_{LH} toward right and left of $PS1$, respectively, i.e.,

$$SSK(x, y) = (PS1(x) + TX_{LH}, PS1(y)),$$
where $K = 2, 3.$ $\quad\quad\quad\quad\quad\quad\quad\quad\quad\quad\quad$ (3.4)

Here, the value of TX_{LH} is subtracted for $SS2$ (right greater Trochanter) and is added for $SS3$ (left greater Trochanter) in the x-coordinate of $PS1$. The lines joining the PFPs and SFPs divide the human body into six segments, i.e., head, torso, right arm, left arm, right leg, and left leg as shown in Fig. 5c.

3.3 FPs Detection within a Segment

Once the human body is segmented, each segment is independently processed for the detection of additional FPs. An overview of the FPs detection within each segment is shown in Fig. 6. The process involves the extraction of the right and the left boundaries, followed by pre-processing for smoothing. Peak and Valley algorithm is then applied to the smoothed boundaries for detection of the segment's FPs. Finally, the FPs are remapped on the segment image.

3.3.1 Segment's Boundary Extraction

To detect the FPs of a segment, the right and left boundaries of the segment are separated. The segment image is scanned from top to bottom, one row at a time. For the ith row, the right and left boundaries are indicated by transitions along the x-axis from high to low ($TX_{HL(i)}$) and low to high ($TX_{LH(i)}$), respectively. The set of right boundaries (RB) and left boundaries (LB) of a body segment are denoted as,

$$RB = \{rb_1, rb_2, rb_3 \ldots rb_m\},$$ $\quad\quad\quad\quad$ (3.5a)
$$LB = \{lb_1, lb_2, lb_3 \ldots lb_n\},$$ $\quad\quad\quad\quad$ (3.5b)

where m and n represents the number of pixels in RB and LB respectively.

3.3.2 Pre-processing

The segment boundaries may contain many false peaks and valleys and needs to be smoothened by a low-pass filter. To

this end, Sagolay filter [33] is applied to the RB and LB of each segment. This filter works by choosing a set of filter coefficients that are equivalent to fitting the data to a polynomial around a single input point, i.e., it performs a local polynomial regression. Since the contours of different segments vary in the human body, a low-pass filter of single order cannot be used for smoothing the whole body contour. Filters of different orders are, therefore, required for each segment to remove the false peaks and valleys and to improve the detection accuracy of FPs.

3.3.3 Peak and Valley Detection

The peaks and valleys of the smoothed boundaries of the segments are detected by using the first-order derivatives as the local maxima and minima respectively. A maxima is associated with a change in the slope from positive to negative, while a minima is associated with a change in the slope from negative to positive [31]. First-order derivatives of RB and LB are

$$drb_i = rb_{i+1} - rb_i \text{ and } dlb_j = lb_{j+1} - lb_j,$$ $\quad$ (3.6)

where $i = 1 \ldots m - 1$ and $j = 1 \ldots n - 1$. The derivative vectors for the left and the right boundaries are given as

$$dRB = \{drb_1, drb_2, drb_3 \ldots drb_{m-1}\},$$ $\quad$ (3.7a)
$$dLB = \{dlb_1, dlb_2, dlb_3 \ldots dlb_{n-1}\}.$$ $\quad$ (3.7b)

The peaks P_r and valleys V_r of the right boundaries (RBs) are detected from dRB as

$$P_r = \{rb_i | drb_i \geq 0 \cap drb_{i+1} < 0\}, \forall_i = 1, 2 \ldots m - 1,$$
$\quad\quad\quad\quad\quad\quad\quad\quad\quad\quad\quad\quad\quad\quad$ (3.8)
$$V_r = \{rb_i | drb_i \leq 0 \cap drb_{i+1} \rangle 0\}, \forall_l = 1, 2 \ldots m - 1.$$
$\quad\quad\quad\quad\quad\quad\quad\quad\quad\quad\quad\quad\quad\quad$ (3.9)

P_l and V_l of the left boundaries (LBs) are similarly calculated. The problem of consecutive zeros is handled by taking the median index of the consecutive zero points.

A series of FPs from six segments of a human body frontal image are detected. The FPs of ears and neck are detected from RB and LB of head as illustrated in Fig. 7a. These include the left ear ($FP1$), the left side of the neck ($FP2$), the
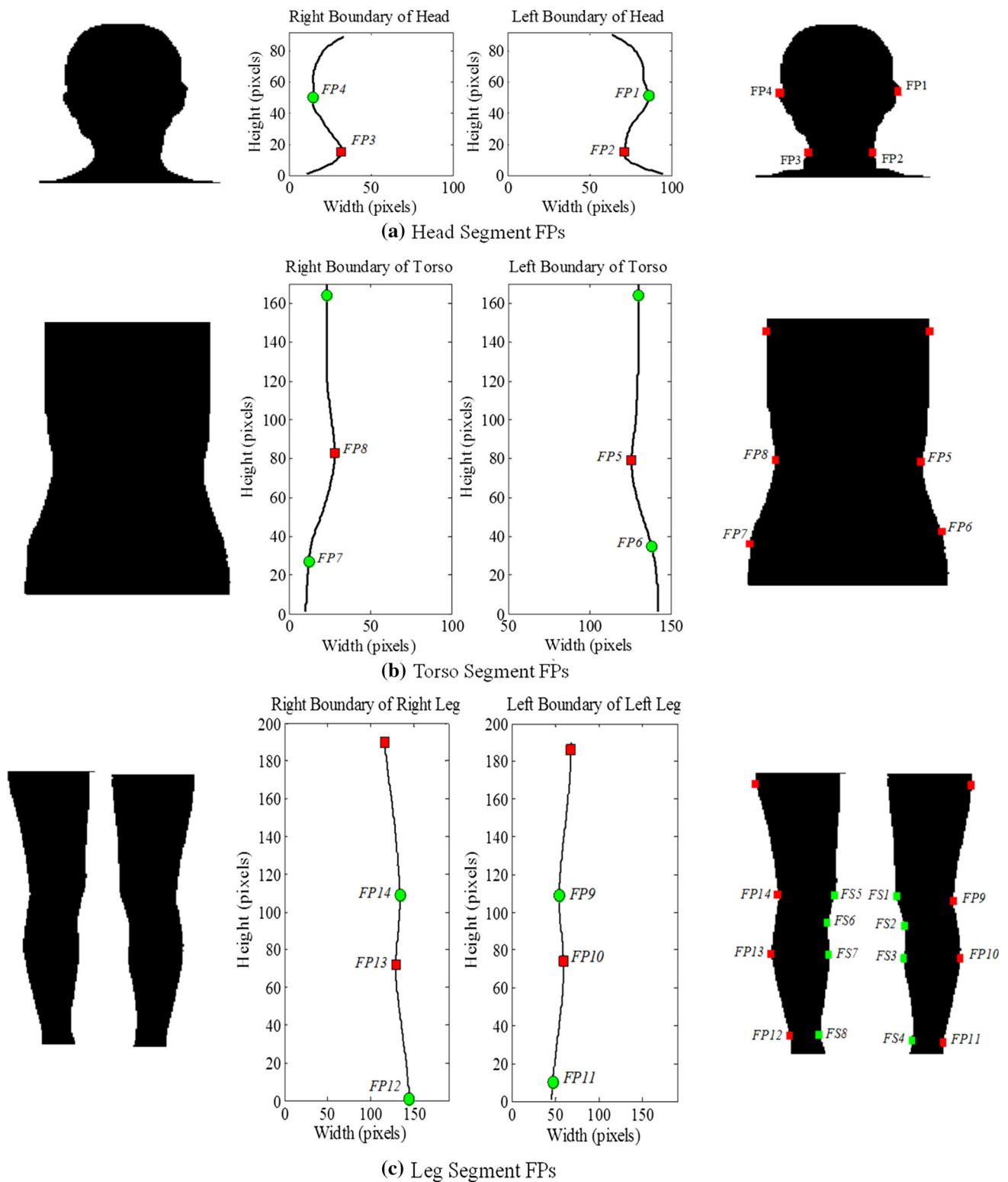
(a) Head Segment FPs

(b) Torso Segment FPs

(c) Leg Segment FPs

Fig. 7 Mapping of segment FPs on segment images

right side of the neck ($FP3$) and the right ear ($FP4$). Additional FPs are detected by processing the *LB* and *RB* of the torso, i.e., the right side of the waist ($FP8$), the left side of the

waist ($FP5$), the right iliac crest ($FP7$) and the left iliac crest ($FP6$) as illustrated in Fig. 7b. For the detection of the FPs from the leg segments, the exterior boundaries are similarly
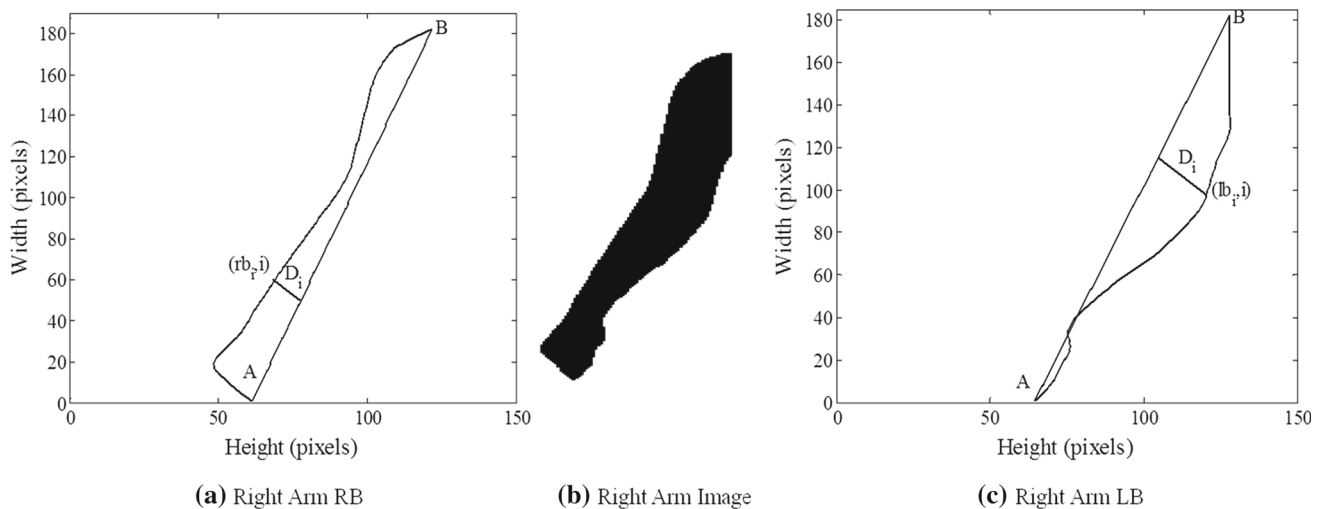
Fig. 8 RB and LB of right arm connected with line AB

processed as illustrated in Fig. 7c. The right-left knee exterior ($FP14$, $FP9$), the right-left shank exterior ($FP13$, $FP10$), and the right-left lateral malleolus ($FP12$, $FP11$) are the important FPs detected. The horizontal projection of the PFPs on the opposite segment boundaries results in detection of eight secondary FPs, i.e., the right-left knee interior ($FS5$, $FS1$), the right-left shank interior ($FS7$, $FS3$), the right-left mid shank-knee interior($FS6$, $FS2$), and the right-left medial malleolus ($FS8$, $FS4$) as shown in Fig. 7c.

3.4 Arms FPs Detection

The FPs of arms cannot be detected directly by applying peak and valley algorithm due to the slanting orientation of arms in the frontal view. Therefore, additional pre-processing is required in order to reorient the *RB* and *LB* so that the arm axis can be considered horizontal. The two end points of *RB* and *LB* are connected with the help of a straight line*AB* as shown in Fig. 8a, c.

The perpendicular distance d_i from the line AB ($ax + by + c = 0$) to the ith point (rb_i, i) on RB is calculated as [34],

$$d_i\left(ax+by+c = 0, (rb_i, i)\right) = \frac{|a\left(rb_i\right) + bi + c|}{\sqrt{a^2 + b^2}}, \quad (3.10)$$

where a, b and c are the coefficients of the straight line AB. The distance D is defined as

$$D_i = \{d_1, d_2, d_3 \ldots d_n\}. \quad (3.11)$$

The peak and valley detection algorithm explained in Sect. 3.3.3 is now applied on Di as shown in Fig. 9a, b. The detected FPs of Di are mapped on RB and LB as shown in Fig. 9c, d. Finally, the FPs ($FP15$–$FP22$) of *RB* and *LB* are remapped on the segment arm image as shown in Fig. 9e.

The FPs ($FP23$–$FP30$) are detected from the left arm using the same procedure.

3.5 Lateral View FPs Detection

For detection of FPs from the lateral view, the input image is preprocessed as described in Sect. 3.1. In the lateral image, the arms are pressed along the body; therefore, it is treated as a single segment and body segmentation is not required for the FPs detection. The *LB* and *RB* extraction and the FPs detection is done using the procedure explained earlier in Sects. 3.3.1–3.3.3. From lateral view 24 FPs (LP1–LP24) are detected as shown in Fig. 10.

4 Results and Discussion

The performance of the proposed algorithm is tested by using 45 test subjects, both males and females, of different age groups with the BMI varying between 18 and 35 as mentioned in Table 1. All the images are taken under the controlled ambient conditions and the special clothes are used which helped to make the body contours more visible. Additionally, caps are used for the subjects with longer hair so that the neck and shoulder region silhouette are clearly visible. These images are then processed using algorithms implemented in MATLAB.

The proposed method automatically detects a total of 70 FPs, which includes 46 FPs from frontal (excluding feet and open hands) and 24 FPs from lateral image views as shown in Tables 2 and 3, respectively. These FPs are detected in two phases. In the first phase, the FPs are detected using the areas between arms and legs which resulted in the segmentation of human body into six regions. In the second phase, the
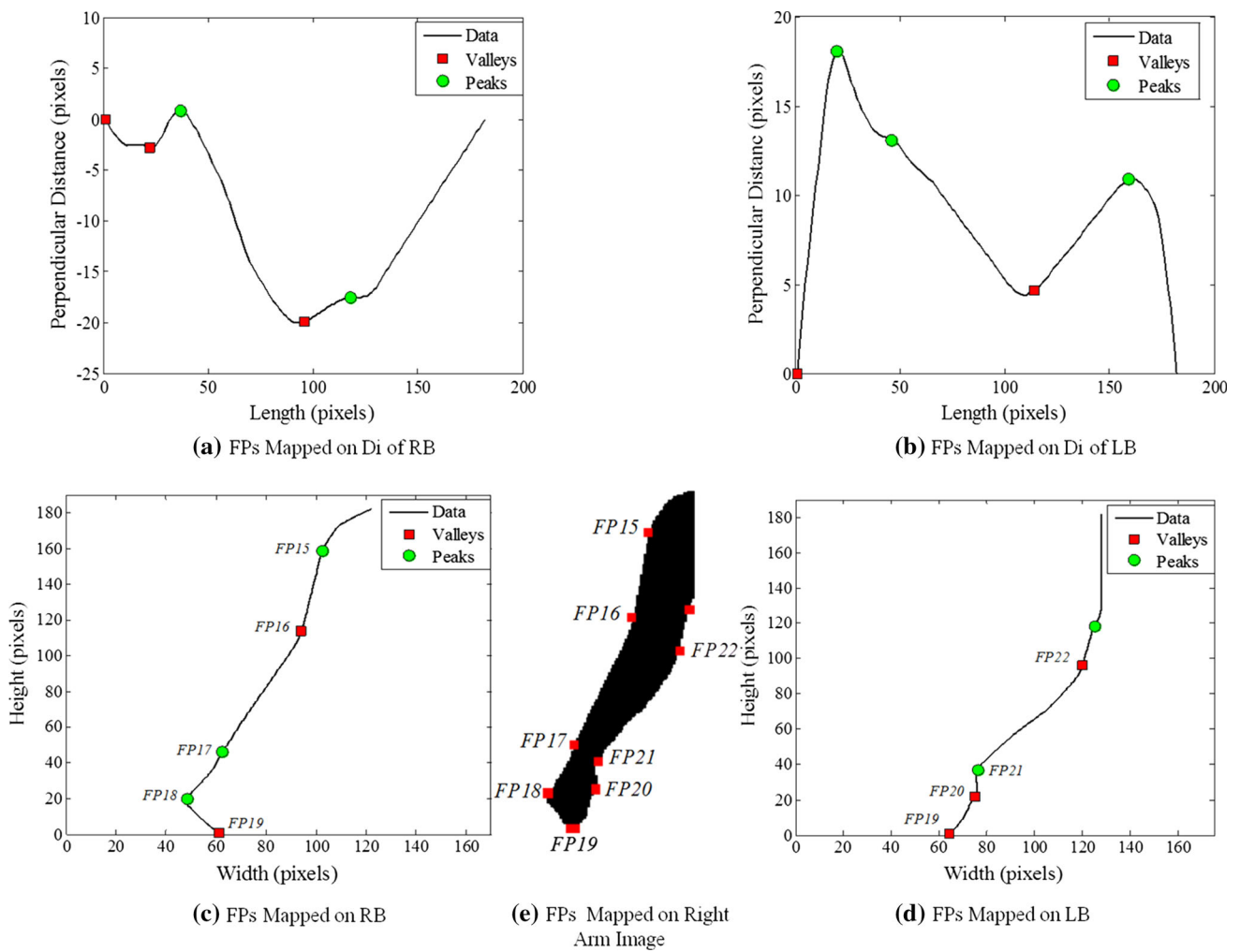
(a) FPs Mapped on Di of RB

(b) FPs Mapped on Di of LB

(c) FPs Mapped on RB

(e) FPs Mapped on Right Arm Image

(d) FPs Mapped on LB

Fig. 9 Mapping of detected FPs on Arm image

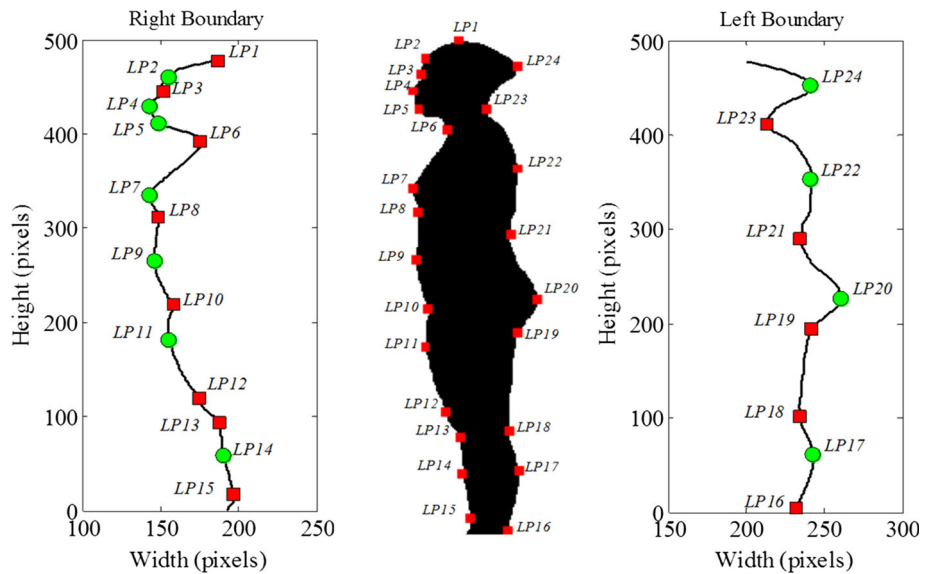**Fig. 10** FPs LP1–LP24 detected from the lateral view

Table 2 Comparing accuracy of the proposed method to the previous methods based on frontal view images

Body part	Fiducial points (frontal view)	Proposed method Right	Proposed method Left	Lin et al. [26] Right	Lin et al. [26] Left	Seo et al. [23]	Meunier et al. [25]	Lee et al. [24]
Head	Head top (SS1)	✓		✓			✓	
	Left ear and Right ear (FP1, FP4)	✓	✓	✓	✓			✓
	Right neck and Left neck (FP3, FP2)	✓	✓	✓	✓	✓	✓	✓
Shoulder	Right clavical and Left clavical (SS2, SS3)	✓	✓	✓	✓			
	Right acromion and Left acromion (FP15, FP30)	✓	✓				✓	✓
Elbow	Right elbow exterior and left elbow exterior (FP16, FP29)	✓	✓					
	Right elbow interior and Left elbow interior (FP22, FP23)	✓	✓					
Wrist	Right radial styloid and Left radial styloid (FP17, FP28)	✓	✓	✓	✓	✓	✓	✓
	Right ulnar styloid and Left ulnar styloid (FP21, FP24)	✓	✓	✓	✓	✓		✓
Hands	Right and left trapezoid, (FP18, FP27)	✓	✓		✓			
	Right and left trapezium, (FP20, FP25)	✓	✓		✓			
	Right and left thumb tip (FP19, FP26)	✓	✓		✓			
Chest	Right armpit, left armpit (PS2, PS3)	✓	✓	✓	✓	✓	✓	✓
Abdomen	Right waist, left waist (FP8, FP5)	✓	✓	✓	✓	✓	✓	✓
Hip	Right greater trochanter, Left greater trochanter (SS4, SS5)	✓	✓	✓	✓	✓	✓	✓
	Right iliac crest, left iliac crest (FP7, FP6)	✓	✓	✓	✓			
Thigh-Knee	Crotch (PS1)	✓		✓		✓		✓
Knee-Shank	Right knee interior and Left knee interior (FS5, FS1)	✓	✓		✓			
	Right knee exterior and Left knee exterior (FP14, FP9)	✓	✓		✓			
	Right shank exterior and Left shank exterior (FP13, FP10)	✓	✓		✓			
	Right shank interior and Left shank interior (FS7, FS3)	✓	✓		✓			
	mid right shank-knee interior and mid left shank-knee interior (FS6, FS2)	✓	✓					
Ankle	Left lateral malleolus and left medial malleolus (FP11, FS4)	✓	✓	✓	✓	✓		✓
	Right lateral malleolus and right medial malleolus (FP12, FS8)	✓	✓		✓			
Total	FPs	46		26		13	13	19

Table 3 Comparing accuracy of the proposed method to the previous methods based on lateral view images

| Body part	Fiducial points	Proposed method	Lin et al. [26]	Seo et al. [23]	Meunier et al. [25]	Lee et al. [24]
Head	Head Top (LP1)	✓	✓		✓	
	Glabella (LP2)	✓	✓			
	Head Posterior (LP24)	✓	✓			
	Eye (LP3)	✓				
	Nose tip (LP4)	✓				
	Chin (LP5)	✓				
Neck	Neck Anterior and Posterior (LP6, LP23)	✓	✓	✓	✓	✓
Torso	Bust Point (LP7)	✓	✓		✓	✓
	Turning Point (LP8)	✓	✓			
	Waist Level (LP9)	✓	✓	✓	✓	✓
	Interior Inferior Iliac spine (ASIS) (LP10)	✓	✓			
	Buttock Point (LP20)	✓	✓		✓	✓
	Waist Level of Back (LP21)	✓	✓	✓	✓	✓
	Backside (LP22)	✓	✓		✓	✓
Legs	Thigh (LP11)	✓	✓			
	Upper Knee (LP12)	✓	✓			
	Lower Knee (LP13)	✓	✓			
	Shank Anterior and Shank Posterior (LP14, LP17)	✓				
	Ankle Anterior and Ankle Posterior (LP15, LP16)	✓	✓	✓		✓
	Popliteal Fosa (LP18)	✓	✓			
	Lowest Point of Hip (LP19)	✓	✓			
Total	FPs	24	18	6	8	9
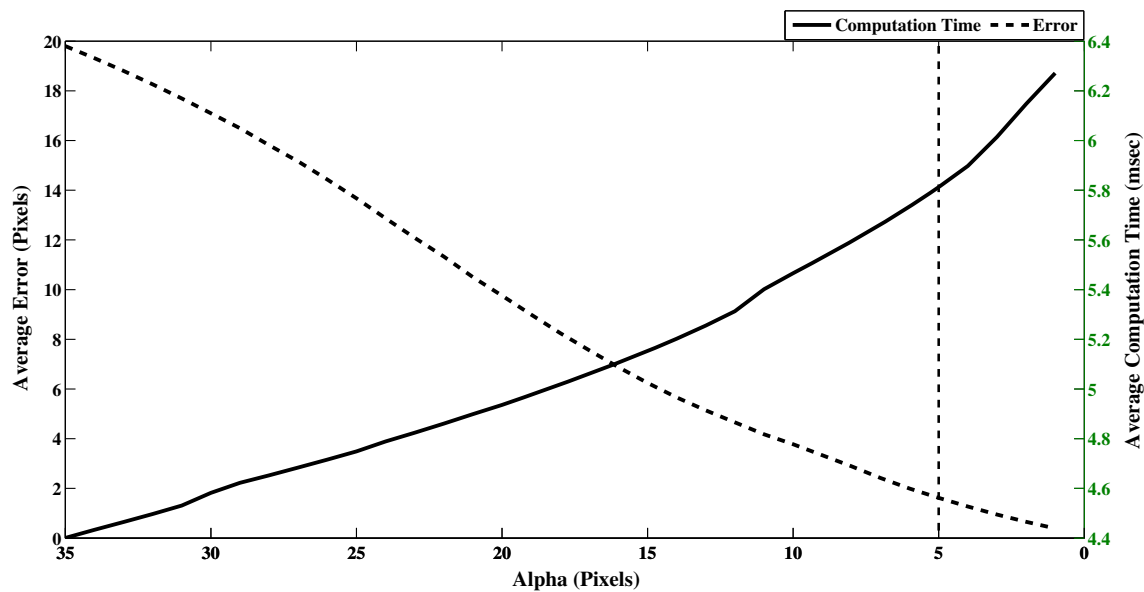
Fig. 11 Average error and average computation time with different values of α

remaining FPs are detected from each of these regions by extracting their boundaries and then marking all the maxima and minima of each boundary as FPs.

The value of α for detection of PFPs and segmentation is validated by testing on 45 subjects. Figure 11 shows the average error and computation time for different target values of α for the armpit region. The Euclidean distance between a detected FP to the manually marked FP is defined as the error measure. The detected FP approaches the manually marked FP as the value of α decreases, but at the cost of increase in the computational time. A value of $\alpha = 5$ is adopted which provides the acceptable average error of 2 pixels and is marked by a vertical dashed line as shown in Fig. 11.

Tables 2 and 3 also shows the comparison of detected FPs with earlier methods in the literature [23–26]. The proposed algorithm accurately detects a greater number of FPs in the head, arm and leg regions as shown in Tables 2 and 3. Also, additional FPs from the head region ($LP3, LP4, LP5$) are detected from the lateral view. Similarly, ($FS6, FS2, FP3, FP7$) in the legs are detected successfully, whereas the state-of-the-art method Lin's technique [26] failed to detect these FPs because of a fixed directional change of 90^0 or 45^0 used from code value of previously detected FPs. Besides, a separate algorithm for the detection of ($FP15, FP16, FP17, FP18, FP20, FP21, FP22$) in the elbow region of the arms is proposed. Some of these FPs ($FP16, FP22$) are not detected in all the earlier methods listed in Table 2. It should be pointed out that one of the main advantages of the proposed approach is that the FPs in each body part is detected separately, independent of the other FPs. This is not the case in some of the earlier

works such as [26] where the detection of a FP depends on the previous FP and may result in error propagation, i.e., if any FP is detected incorrectly, it also affects the subsequent detection of other FPs.

The proposed method not only identifies the positions of the detected FPs but also associated them with the body parts automatically through segmentation. The segmentation of a human body into six regions helps in extraction of anthropometric parameters like area, length, breadth, ratios of each body segment. Moreover, the detected FPs are also useful in the human body posture evaluation. FPs like $LP6, LP7, LP10, LP20, LP21, LP23, LP24$ are used for measuring three spinal angles cervical, thoracic and lumbar in order to evaluate posture disorders in the torso region [9,35–37].

The accuracy of a detected FP is calculated as the Euclidean distance of the manually marked FP from the automatically detected FP. The detection accuracy of the proposed algorithm is compared with Lin's algorithm [26] using the box plot as shown in Fig. 12. Initially, all FPs of each subject are marked manually. The Euclidean distances of the manually marked FPs from automatically detected FPs are then calculated to find the detection error of all the test subjects. Finally, the screen calibration values are used to convert detection error to real values in centimeters. The FP results for the right and left human body halves have been merged due to its symmetry. In Fig. 12a, b, the ends of each box represent the first (25th percentile) and third (75th percentile) quartiles, whereas the median (50th percentile) is marked by a horizontal line inside the box. The whiskers are the two lines outside the box that extend to the highest and
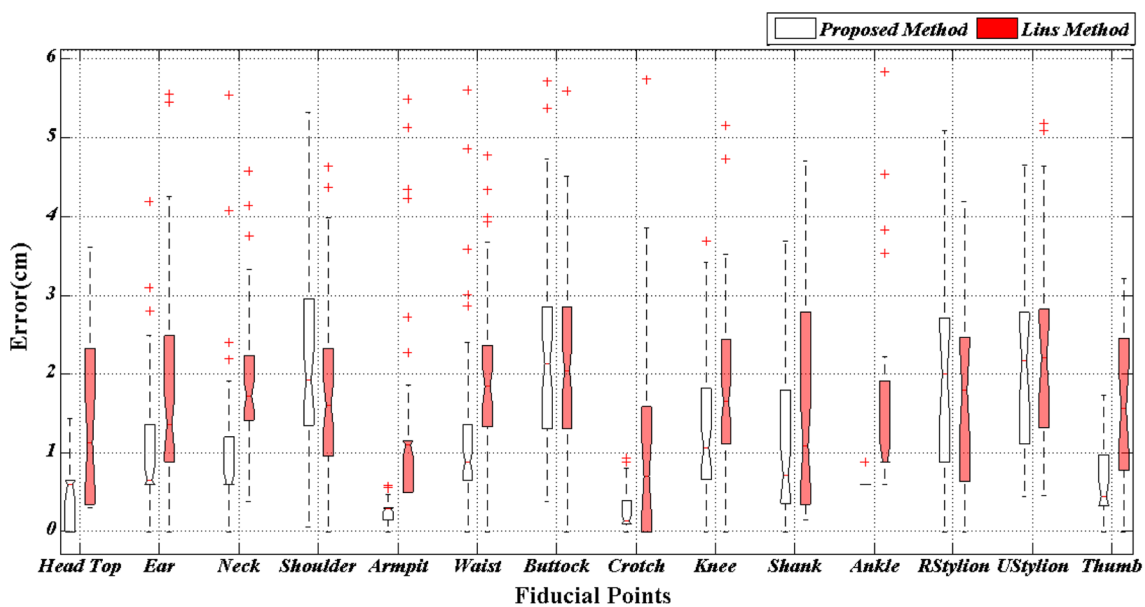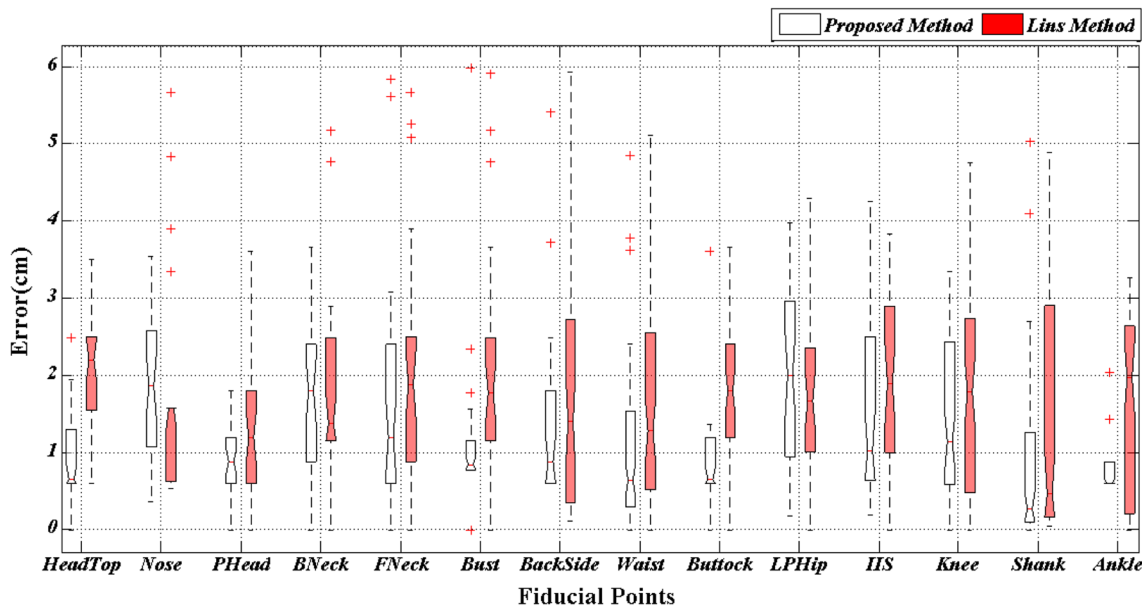
Fig. 12 Comparing accuracy of the FPs detected by the proposed method with the Lin's method. **a** Boxplot of the detection accuracy for the frontal view. **b** Boxplot of the detection accuracy for the lateral view

lowest observations. Outliers are the data points with values beyond the ends of the whiskers and are displayed with a + sign. It is found that the detection error of the proposed algorithm is much lower for the majority of the FPs (20 out of 26 in the frontal view). However, in a few regions like the shoulder, buttock, and wrist (6 FPs), the accuracy of Lin's algorithm is better. Similarly, the detection accuracy of lateral view is compared in Fig. 12b. The proposed algorithm also reduces the detection error significantly for the majority of the FPs (15 out of 18 in the lateral view), whereas Lin's

algorithm is more accurate in nose, neck and hip regions. This accurate detection of FPs leads to an accurate detection of anthropometric measurements and evaluation of postural disorders.

The percentage accuracy (PA) of the FPs compared in Fig. 12a, b is also calculated. The PA of kth FP (PA_k) is evaluated as
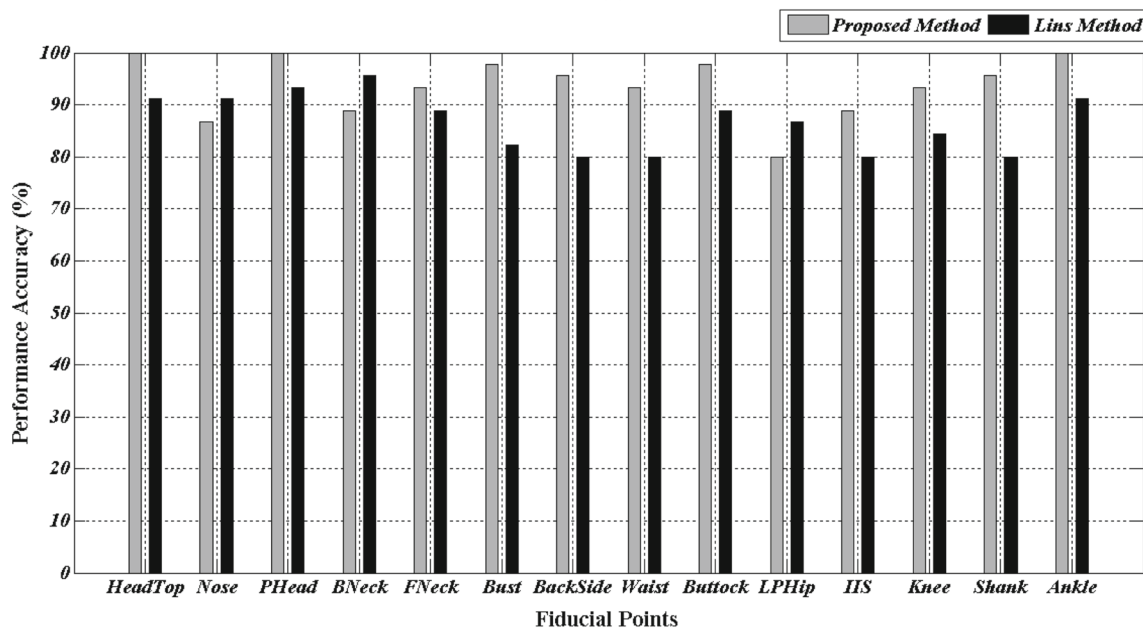
$$PA_k = \left(\frac{M}{N}\right) \times 100, \tag{4.1}$$

Table 4 Comparison of performance accuracy (%) for different values of allowable error

View:	Frontal view		Lateral view	
Methods:	Proposed method (PA)	Lin et al. [26] (PA)	Proposed method (PA)	Lin et al. [26] (PA)
AE				
3 cm	91	86	94	87
2 cm	79	65	80	62
1 cm	60	32	54	32
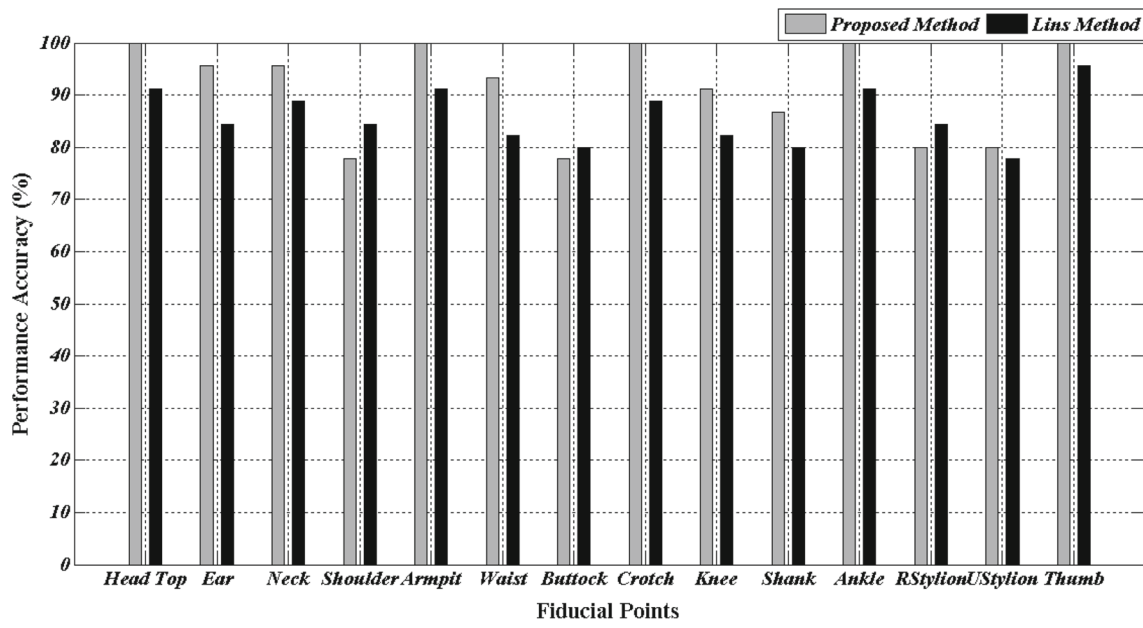
Fig. 13 Percentage accuracy (PA) of the FPs detected by the proposed method and Lin's method for AE threshold value of 3 cm. **a** Frontal view, **b** lateral view

where $N = 45$, is the total number of subjects and M is the number of subjects with detection error less than the threshold set for allowable error (AE). Table 4 compares the average PA of proposed algorithm and Lin's algorithm for different threshold values of AE. For each value of AE, the average value of PA is calculated for all the frontal view FPs, shown in Fig. 12a, and for all the lateral view FPs, shown in Fig. 12b. The proposed method has performed better for all values of AE when compared to Lin's method. Moreover, if AE is decreased from 3 to 1 cm, the average PA for proposed method and Lin's method has degraded 1.6 and 2.7 times respectively. These results show that the performance of Lin's method is more susceptible to AE. Finally, Fig. 13a, b shows the PA of each FP detected by the proposed algorithm and Lin's algorithm for the AE value of 3 cm. The proposed algorithm performs better for 20 out of 26 FPs, and 15 out of 18 FPs for the frontal and lateral views, respectively. Although the complexity of the proposed algorithm is comparable to that of Lin's method, the PA and detection accuracy for more than 80% of the detected FPs has improved. Hence, the statistical analysis indicates that the proposed method is more accurate and consistent as compared to Lin's method.

The proposed system has some limitations, which in fact are the limitations of all such systems [23–26] where the objective is to detect the significant points on the human body using 2D imaging system. For the accurate detection of FPs and the extraction of the human body from the image, a blue background screen is used. Since the blue color is not a part of any skin color tone, this results in a more accurate segmentation of human body. Additionally, markers on the screen are used for measurement of real coordinates of FPs. Special measurement attires have been used while taking photographs so that most of the curves of the body are clearly visible which are helpful for the detection of body FPs. The tight dress is also helpful in avoiding false peaks and valleys which appear if the subject is under more apparel. For the accurate detection of FPs, specific postures are maintained for frontal and lateral views while taking the photographs, which are standard postures for all such applications [23–26].

5 Conclusions and Future Work

In this paper, automated human body FPs detection and segmentation method using 2D images is proposed. The proposed method divides the 2D image of a human body into six segments and associates the FPs with the corresponding body parts accurately. All the FPs are detected and evaluated separately, thereby avoiding error propagation. The proposed work is tested on a dataset from 45 subjects including both male and female genders. A total of 70 FPs including additional FPs in the arm, head and leg regions are detected. The detection accuracy of the proposed method is compared with the existing work in the literature and verified against the manual readings. The detection error is very small for the majority of the FPs. The percentage accuracy of the detected FPs is calculated and compared with existing work, and it is observed that the proposed algorithm performs better for the majority of the FPs.

The presented work of detecting the FPs can be extended in future for the automatic measurement of anthropometric dimensions, constructing 3D digital human models, for gender recognition, and for automatic detection of postural disorders. Furthermore, the existing algorithms can be made more robust for detecting and approximating the FPs of the subjects under different (more loose) apparels.

References

1. Leong, I.F.; Fang, J.J.; Tsai, M.J.: Automatic body feature extraction from a marker-less scanned human body. Comput. Aided Des. **39**(7), 568–582 (2007)
2. Lin, Y.L.; Wang, M.J.J.: Constructing 3D human model from 2D images. In: 2010 IEEE 17th International Conference on Industrial Engineering and Engineering Management (IE& EM), pp. 1902–1906. IEEE (2010)
3. Lin, Y.L.; Wang, M.J.J.: Constructing 3D human model from front and side images. Expert Syst. Appl. **39**(5), 5012–5018 (2012)
4. Rahman, S.A.; Cho, S.Y.; Leung, M.K.: Recognising human actions by analysing negative spaces. Comput. Vis. IET **6**(3), 197–213 (2012)
5. İkizler, N.; Forsyth, D.A.: Searching for complex human activities with no visual examples. Int. J. Comput. Vis. **80**(3), 337–357 (2008)
6. Bregler, C.: Learning and recognizing human dynamics in video sequences. In: 1997 IEEE Computer Society Conference on Computer Vision and Pattern Recognition, 1997. Proceedings, pp. 568–574. IEEE (1997)
7. Lin, Y.L.; Wang, M.J.J.: Automatic feature extraction from front and side images. In: IEEE International Conference on Industrial Engineering and Engineering Management, 2008. IEEM 2008, pp. 1949–1953. IEEE (2008)
8. Han, H.; Nam, Y.: Automatic body landmark identification for various body figures. Int. J. Ind. Ergon. **41**(6), 592–606 (2011)
9. Wang, C.C.: Parameterization and parametric design of mannequins. Comput. Aided Des. **37**(1), 83–98 (2005)
10. Uhm, T.; Park, H.; Park, J.I.: Fully vision-based automatic human body measurement system for apparel application. Measurement **61**, 169–179 (2015)
11. Yamada, H.; Hirose, M.; Kanamori, Y.; Mitani, J.; Fukui, Y.: Image-based virtual fitting system with garment image reshaping. In: 2014 International Conference on Cyberworlds (CW), pp. 47–54. IEEE (2014)
12. Dunk, N.M.; Lalonde, J.; Callaghan, J.P.: Implications for the use of postural analysis as a clinical diagnostic tool: reliability of quantifying upright standing spinal postures from photographic images. J. Manip. Physiol. Ther. **28**(6), 386–392 (2005)
13. Yu, C.Y.; Lo, Y.H.; Chiou, W.K.: The 3D scanner for measuring body surface area: a simplified calculation in the Chinese adult. Appl. Ergon. **34**(3), 273–278 (2003)
14. Ju, X.; Werghi, N.; Siebert, J.P.: Automatic segmentation of 3D human body scans. In: Proceedings of IASTED International Conference on Computer Graphics and Imaging 2000 (CGIM 2000), Las Vegas, (2000)

15. Robinette, K.M.; Daanen, H.; Paquet, E.: The CAESAR project: a 3-D surface anthropometry survey. In: Second International Conference on 3-D Digital Imaging and Modeling, 1999. Proceedings, pp. 380–386. IEEE (1999)

16. Xin-juan, Z.; Xiao-ya, X.: Human body shapes modeling and feature points location based on ASM for virtual fitting. In: 2016 Sixth International Conference on Information Science and Technology (ICIST), pp. 476–481. IEEE (2016)

17. Simmons, K.P.; Istook, C.L.: Comparison of 3-Dimensional body scanners for use potential. Text. Asia **32**(5), 48–52 (2001)

18. Nurre, J.H.; Connor, J.; Lewark, E.; Collier, J.S.: On segmenting the three-dimensional scan data of a human body. IEEE Trans. Med. Imaging **19**(8), 787–797 (2000)

19. Al-Ali, S.; Milanova, M.; Al-Rizzo, H.; Fox, V.L.: Human action recognition: contour-based and Silhouette-based approaches. In: Favorskaya, M.N., Jain, L.C. (eds.) Computer Vision in Control Systems, vol. 2, pp. 11–47. Springer International Publishing, Switzerland (2015)

20. Lowe, D.G.: Distinctive image features from scale-invariant keypoints. Int. J. Comput. Vis. **60**(2), 91–110 (2004)

21. Mikolajczyk, K.; Schmid, C.: Scale & affine invariant interest point detectors. Int. J. Comput. Vis. **60**(1), 63–86 (2004)

22. Bay, H.; Tuytelaars, T.; Van Gool, L.: SURF: speeded up robust features. In: European Conference on Computer Vision, pp. 404–417. Springer, Berlin (2006)

23. Seo, H.; Yeo, Y.I.; Wohn, K.: 3D body reconstruction from photos based on range scan. In: Pan, Z., Aylett, R., Diener, H., Jin, X., Göbel, S., Li, L. (eds.) Technologies for e-Learning and Digital Entertainment, pp. 849–860. Springer, Berlin, Heidelberg (2006)

24. Lee, W.; Gu, J.; Magnenat-Thalmann, N.: Generating animatable 3D virtual humans from photographs. Comput. Graph. Forum **19**(3), 1–10 (2000)

25. Meunier, P.; Yin, S.: Performance of a 2D image-based anthropometric measurement and clothing sizing system. Appl. Ergon. **31**(5), 445–451 (2000)

26. Lin, Y.L.; Wang, M.J.J.: Automated body feature extraction from 2D images. Expert Syst. Appl. **38**(3), 2585–2591 (2011)

27. Canny, J.: A computational approach to edge detection. IEEE Trans. Pattern Anal. Mach. Intell. **6**, 679–698 (1986)

28. Freeman, H.; Davis, L.S.: A corner-finding algorithm for chain-coded curves. IEEE Trans. Comput. **3**, 297–303 (1977)

29. Bradski, G.; Kaehler, A.: Learning OpenCV: Computer Vision with the OpenCV Library. O'Reilly Media, Inc., Sebastopol (2008)

30. Gonzalez, R.C.; Woods, R.E.: Digital Image Processing, 3rd edn. Pearson Prentice Hall, ISBN: 9780131687288 (2008)

31. Nopiah, Z.M.; Khairir, M.I.; Abdullah, S.; Nizwan, C.K.E.: Peak-valley segmentation algorithm for fatigue time series data. WSEAS Trans. Math. **7**(12), 698–707 (2008)

32. Manresa-Yee, C.; Varona, J.; Mas, R.; Perales, F.J.: Hand tracking and gesture recognition for human-computer interaction. Electron. Lett. Comput. Vis. Image Anal. **5**(3), 96–104 (2005)

33. Schafer, R.W.: What is a Savitzky–Golay filter? [lecture notes]. IEEE Signal Process. Mag. **28**(4), 111–117 (2011)

34. Larson, R.; Hostetler, R.: Precalculus: A Concise Course. Houghton Mifflin Co, Boston, ISBN: 0-618-62719-7 (2007)

35. Duong, L.; Mac-Thiong, J.M.; Labelle, H.: Real time noninvasive assessment of external trunk geometry during surgical correction of adolescent idiopathic scoliosis. Scoliosis **4**(1), 5 (2009)

36. Jaremko, J.L.; Poncet, P.; Ronsky, J.; Harder, J.; Dansereau, J.; Labelle, H.; Zernicke, R.F.: Indices of torso asymmetry related to spinal deformity in scoliosis. Clin. Biomech. **17**(8), 559–568 (2002)

37. Berryman, F.; Pynsent, P.; Fairbank, J.; Disney, S.: A new system for measuring three-dimensional back shape in scoliosis. Eur. Spine J. **17**(5), 663–672 (2008)